Supplementary information for:

Nanostructured Hybrid Catalysts Empower the Artificial Leaf for Solar-Driven Ammonia Production from Nitrate

Chen Han[1], Caixia Li[2], Jodie A. Yuwono[3], Ziheng Liu[2], Kaiwen Sun[2], Kai Wang[4], Guojun He[2], Jialiang Huang[2], Priyank V. Kumar[1], Jitraporn Vongsvivut[5], Jialin Cong[2], Hamid Mehrvarz[2], Zhaojun Han[1], Xunyu Lu[1], Jian Pan[1]*, Xiaojing Hao[2]*, Rose Amal[1]*

[1]School of Chemical Engineering, University of New South Wales, Sydney, Australia.

[2]School of Photovoltaic and Renewable Energy Engineering, University of New South Wales, Sydney, Australia.

[3]School of Chemical Engineering, The University of Adelaide, Adelaide, Australia.

[4]WA School of Mines: Minerals, Energy and Chemical Engineering, Curtin University, Perth, Australia.

[5]Australian Nuclear Science and Technology Organisation, Australian Synchrotron, Clayton, Australia.

*e-mail: r.amal@unsw.edu.au, jian.pan@unsw.edu.au and xj.hao@unsw.edu.au.

Methods

Materials

Si solar cell (heterojunction with intrinsic thin-layer, HJT), Cu target (99.99%, AJA international), KNO_3 (≥ 99.0%, Sigma-Aldrich), KOH (90%, Sigma-Aldrich), NaOH (98%, Chem-supply Australia), $(NH_4)_2S_2O_8$ (≥98.0%, Sigma-Aldrich), $Co(NO_3)_2{\cdot}6H_2O$ (98%, Sigma-Aldrich), $CoCl_2$ (97%, Sigma-Aldrich), 2-Methylimidazole (99%, Sigma-Aldrich), D_2O (99.9%, Cambridge Isotope Laboratories), $K^{15}NO_3$ (98.0 atom% ^{15}N, Sigma-Aldrich), KNO_2 (98%, Ajax Finechem), HCl (32%, RCI Labscan), H_2SO_4 (98%, Supelco), $H_2PtCl_6{\cdot}xH_2O$ (≥ 99.9%, Sigma-Aldrich), glycerol (99.5%, Chem-supply Australia), NaCl (≥ 99.0%, Sigma-Aldrich), ethanol (100%, Chem-supply Australia), isopropyl alcohol (70%, Chem-supply Australia), anion exchange membrane (Dioxide Materials), Milli-Q water (18.2 MΩ·cm), H_2 (Coregas), Ar (Coregas).

The photoelectrodes in regular size and large-scale size (25 cm^2) were synthesized on HJT solar cell without and with metallization, respectively.

Photocathode synthesis

The Cu nanowires layer (Cu-NSTL) was synthesized on Si cell by a facile process. Firstly, Si cell surface was cleaned by ozone plasma, which can enhance the adhesion between the outer ITO layer on Si cell with sputtered Cu. Then, a Cu layer of around 500 nm was fabricated on n-type side surface by sputtering (p-Cu-Si), and transferred to $Cu(OH)_2$ NWs by a self-etching process in 1 M NaOH and 0.05 M $(NH_4)_2S_2O_8$ for 15 min. The synthesized $Cu(OH)_2$ NWs were annealed in 180 ℃ Ar/H_2 to produce Cu NWs (Cu-Si). For the fabrication of $Cu/Co(OH)_2$-Si, thin $Co(OH)_2$ nanosheets were electrodeposited onto Cu-NSTL in 0.05 M $Co(NO_3)_2{\cdot}6H_2O$ at -1.0 $V_{Ag/Agcl}$ under illumination for 20 s. To synthesis $Co(OH)_2$-Si, the $Co(OH)_2$ nanosheets were electrodeposited directly on the n-type side of Si.

To prepare the large-scale photocathode, after forming Cu-Si structure, a self-assembling method was used to prepare the outer $Co(OH)_2$ layer, which was revised from reported literature.[1] The Cu-Si was treated with a fresh solution mixed with 0.4 M 2-methylimidazole and 0.05 M $CoCl_2$ for 3 hours. The sample was then taken out and immersed in a 0.046 M $CoCl_2$ ethanol solution for 20 min to derive SA-$Cu/Co(OH)_2$-Si.

Photoanode synthesis

The Cu/Pt-Si was synthesized by immersing Cu-Si structure in 1mM H_2PtCl_6 solution for several minutes.

Photoelectrochemical measurements

PEC measurements were obtained with a potentiostat (Autolab) and a gas-tight H-cell reactor. The cathodic and anodic sides were filled with 50 mL of electrolyte and separated by an anion exchange membrane. The illumination was provided by a solar simulator (AM 1.5G, Pico), and the power intensity of the incident light was calibrated to 100 mW cm^{-2} at the surface of reactor window. For the tested photocathodes, the exposed back illuminated area (p-type side) and the front catalytic area (n-type side) were same. The EQE result in Fig. S4 shows the catalytic process-happening side has negligible contribution on light absorption. The performance evaluation, LSV and EIS were collected with Pt foil and Ag/AgCl (KCl_{sat}) as counter and reference electrode, respectively. Before each test, Ar was purged in H-cell for more than 15 min to remove air. A solution with 0.1 M KOH and 0.1 M KNO_3 was used as electrolyte (pH ~ 13.5). No *iR* correction was applied.

The bias-free operation was achieved in a two-photoelectrode device configuration with the catholyte of 0.1 M KOH + 0.1 M KNO_3 and the anolyte of 0.1 M KOH + 0.1 M KNO_3 + 0.1 M glycerol.

Products quantitation

a. Ammonia (as NH_4^+)

The produced ammonia was determined by UV-Vis (UV-3600, Shimadzu). After reaction, 0.5 mL of catholyte was taken and mixed with 0.4 mL of Kit 1, 0.1 mL of Kit 2 and 30 μL of Kit 3, where the content of each Kit is listed below:

Kit 1: 1 M NaOH solution with 5 wt.% salicylic acid and 5 wt.% sodium citrate.

Kit 2: 0.05 M NaClO.

Kit 3: 1 wt.% $C_5FeN_6Na_2O$ (sodium nitroferricyanide).

The mixture was then preserved in dark at room temperature for 1 hour before the UV-Vis testing. The concentration of ammonia can be calculated via the calibration curve (Fig. S6a). In this work, a set of standard solutions with known amount NH_4Cl in 0.1 M KNO_3 and 0.1 M KOH were prepared, and they showed a strong absorbance at around 655 nm.

The $^{14}NH_4^+$ and $^{15}NH_4^+$ products were detected by NMR (Avance III 600MHz Cryo NMR, Bruker) using a water suppression method. Before NMR test, the pH of collected electrolyte needs to be adjusted to around weak acid.

b, Nitrite

50 μL of electrolyte, 50 μL of Griess Reagent and 0.9 mL of Milli-Q water were mixed and kept at room temperature in dark for 0.5 h before the UV-Vis testing. A set of standard solutions with 0.1 M KNO_3, 0.1 M KOH and known concentration of KNO_2 were prepared, with the absorbance at 525 nm to plot the calibration curve (Fig. S6b).

c, H_2

The gas products were determined by gas chromatograph (GC, Model 2010, Shimadzu) equipped with both a thermal conductivity detector (TCD) and flame ionization detector (FID).

d, Formate

The produced formate in glycol oxidation reaction (GOR) was detected by NMR (Avance III 600MHz Cryo NMR, Bruker) with a water suppression method.

Faradic efficiency and yield rate

The Faradic efficiency and yield rate were calculated by the following equations:

$$FE = \frac{ncVF}{Q} \times 100\% \quad (1)$$

$$Y = \frac{cV}{St} \quad (2)$$

Where n is the number of transferred electrons for producing desired products (n=2 for nitrite, n=8 for ammonia, n=8/3 for formate); c is the molar concentration of the product; V is the volume of catholyte/anolyte; F represents the Faraday constant (F=96485.33); Q is the total charge passing the photoelectrode; S is the surface area of photoelectrode; and t is the reaction time.

Solar utilization efficiency

The solar utilization efficiency was calculated by the following equation under bias-free operation:

$$\eta = \frac{J \times V}{P_{incident}} \times 100\% \quad (3)$$

J is the photocurrent density and V is the potential provided by photoelectrodes. $P_{incident}$ is the power intensity of the incident light.

Materials Characterization

FEI Nova NanoSEM450 was employed for SEM imaging and EDX mapping. HR-TEM images and EDX elemental mapping were obtained on a TEM (FEI Titan) with an EDX analyzer at an accelerating voltage of 200 kV. The surface chemical states and energy band structure were analyzed by XPS and UPS (Thermo ESCALAB 250Xi) with a mono-chromated Al Kα radiation source (1486.68 eV) and He I excitation light (21.22 eV). The band gap of photoelectrodes was determined by UV-vis (UV-3600, Shimadzu). XRD patterns were collected on PANalytical Empyrean Thin Film XRD. The X-ray absorption spectroscopy (XAS) measurements were carried out at medium energy X-ray absorption spectroscopy beamline (MEX-1) in transmission mode at ANSTO, Australia.

PV characterization

The TEM specimens were prepared by a plasma FIB (Thermo Fisher Helios G4 PFIB) and a final ion beam polish was applied by Fischione NanoMill 1040 to ensure a clean and fresh surface. The microstructure and compositional profiles were measured using a JEOL F200 (200 kV) cold field-emission gun (FEG) scanning transmission electron microscope equipped with a windowless silicon drift EDX detector. EQE measurements were conducted by utilizing a QEX10 spectral response system (PV measurements, Inc.) calibrated by the National Institute of Standards and Technology (NIST) certified reference Si and Ge photodiodes.

In-situ photoelectrochemical characterization

The in-situ photoelectrochemical SR-PD data were collected in PD beamline at ANSTO, Australia (X-ray energy 21.0005 keV). A custom-designed PEC setup was used during the in-situ SR-PD test.

The in-situ photoelectrochemical Raman spectra were acquired on a Renishaw inVia microscope using 514 nm or 633 nm laser diode as the excitation source. A custom-designed PEC setup was used during the in-situ Raman test.

The in-situ photoelectrochemical SR-IR measurements were carried out in IR beamline at ANSTO, Australia. It has been realized through a homemade 3-electrodes photoelectrochemical cell, with a ZnSe window. The IR station was equipped with an FTIR spectrometer (Bruker 66 v/s) with a KBr beam splitter and Mercury-Cadmium-Telluride (MCT) detector. It coupled with an IR microscope (Bruker Hyperion 3000) with a 20x objective. Each IR adsorption spectrum was acquired in reflection mode by 256 scans at solution of 2 cm^{-1}. The background spectrum was collected at open-circuit voltage before the in-situ PEC test.

Computational method

DFT calculations were implemented using the Vienna ab-initio simulation package (VASP)[2,3] with the core and valence electronic interactions being modelled using the projector augmented wave (PAW) method.[4,5] The Perdew-Burke-Ernzerhof (PBE) exchange-correlation functional[6] was employed. The wavefunction was expanded with a kinetic energy cut-off of 500 eV and a Monkhorst-Pack k-points of 7×7×1 was used. The slab method was used to model Cu (111) and $Co(OH)_2$ (100) surfaces. A vacuum region of 20 Å was introduced in the direction of the z-axis to avoid interactions between periodic images. The zero-point energy and entropic contributions at 298 K as well as the solvation correction for H_2 and H_2O were also considered in the calculations of free reaction energy. Geometrical optimizations were achieved by relaxing all ionic positions and supercell vectors until the Hellman-Feynmann forces were less than 0.03 eV $Å^{-1}$. The dispersion correction was also considered in this study by using DFT-D3 method.[7]

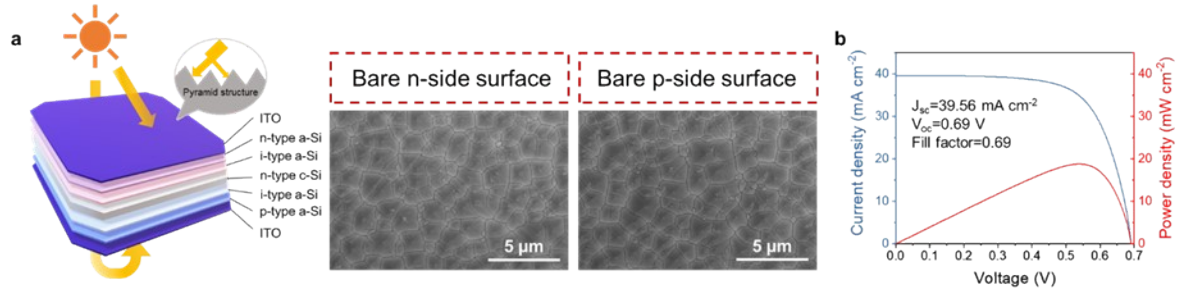

Fig. S1 (a) Schematic illustration of HJT light-absorber and the corresponding SEM images of the bare n- and p-type side surfaces. (b) Electrical characteristics of synthesized photoelectrode.

The near-finished HJT structure has been employed in this work (Fig. S1a), with the configuration of ITO/n-type amorphous silicon (a-Si)/i a-Si/n-type c-Si/i a-Si/p-type a-Si/ITO. It is composed by a sandwich structure with a thin c-Si wafer as the main part of photo-absorber, and the surrounded ultra-thin a-Si layers can reduce recombination losses at the hetero-interface (a-Si/c-Si) of photo-generated charges. The ITO layers on both sides work as transparent electrode, with a thickness of approximately 80 nm. Both the n- and p-type side surfaces feature a special pyramid structure, benefiting for effective photons absorption with less reflection loss. As shown in Fig. S1b, the electrical characteristics of the synthesized photoelectrode are consistent with those of the pure Si solar cell, demonstrating a short-circuit current density (Jsc) of 39.56 mA cm^{-2}, an open-circuit voltage (Voc) of 0.69 V and a fill factor of 0.69. Thus, the Si structure (HJT) with hybrid of c-Si and a-Si demonstrates several advantages on their energy-saving producing technology, less crystalline silicon using, high efficiency, high output photovoltage, and good stability. It has been regarded as low-cost alternative to traditional c-Si solar cell, showing increasing occupation in solar market and expecting with a bright future.

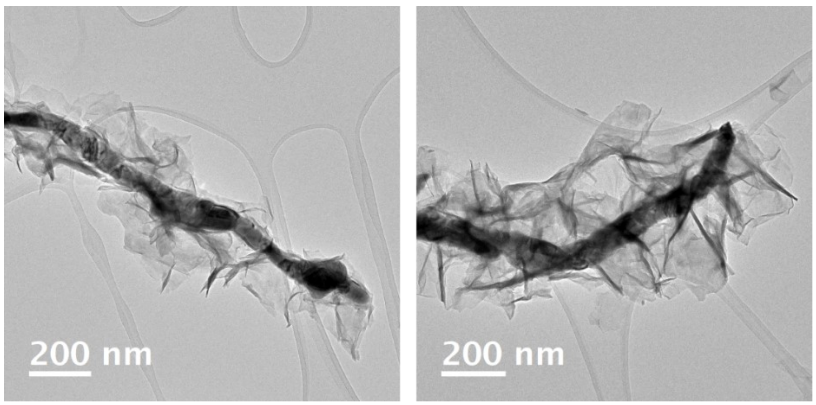

Fig. S2 TEM images of Cu/$Co(OH)_2$-Si.

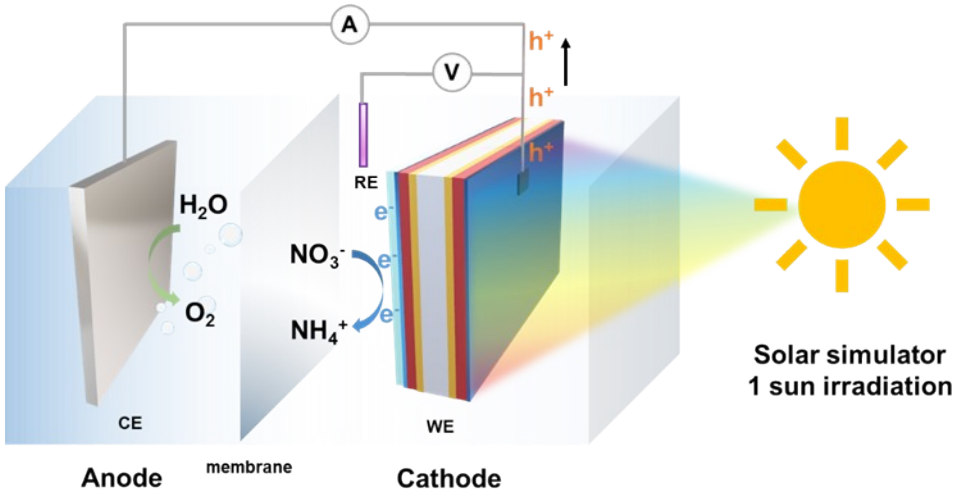

Fig. S3 Schematic illustration of PEC NO_3RR measurement in a 3-electrode H-cell, with the synthesized photoelectrode as the working electrode (WE), Ag/AgCl as the reference electrode (RE) and Pt as the counter electrode (CE).

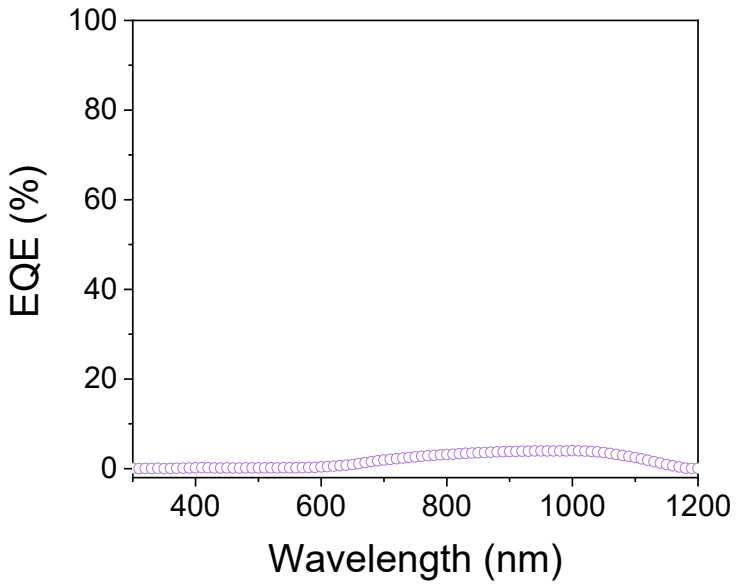

Fig. S4 EQE analysis obtained from the n-type side of Si with Cu-NSTL.

The result indicates that the illumination area of photocathode is equal to the area of p-type side exposure.

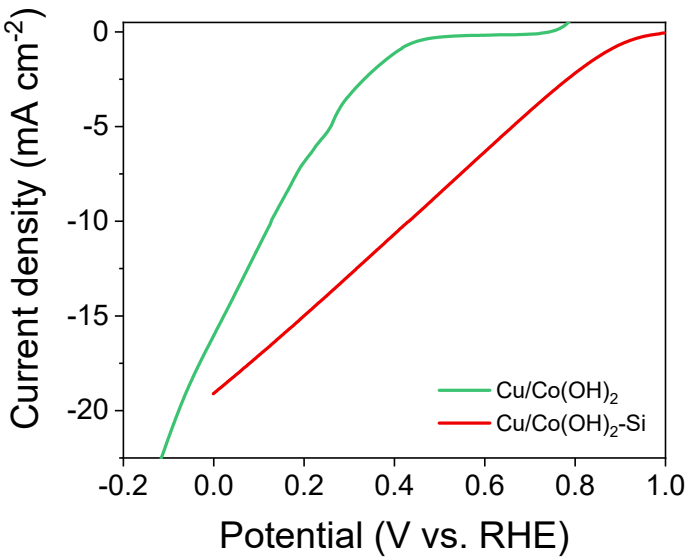

Fig. S5 LSV curves of $Cu/Co(OH)_2$ and $Cu/Co(OH)_2$-Si.

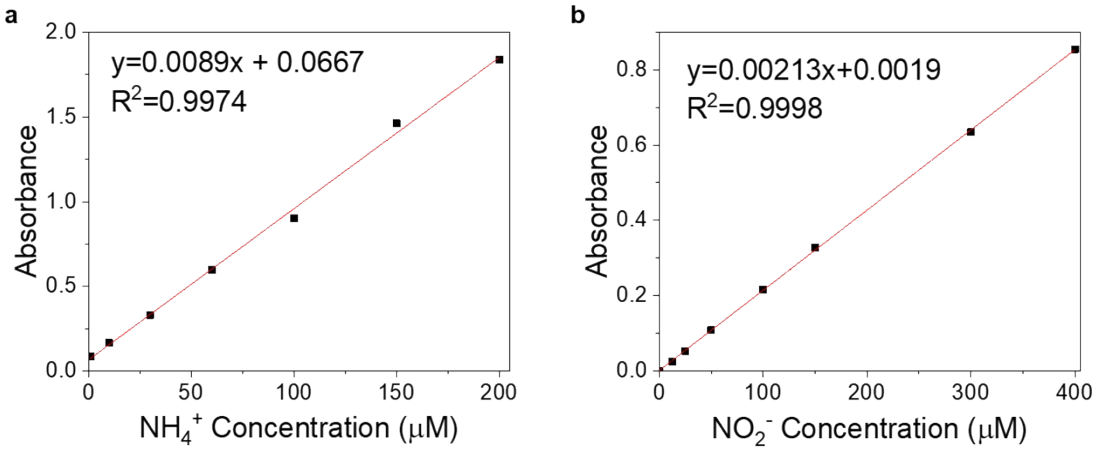

Fig. S6 Calibration curves of (a) ammonia (in NH_4^+ from) and (b) nitrite.

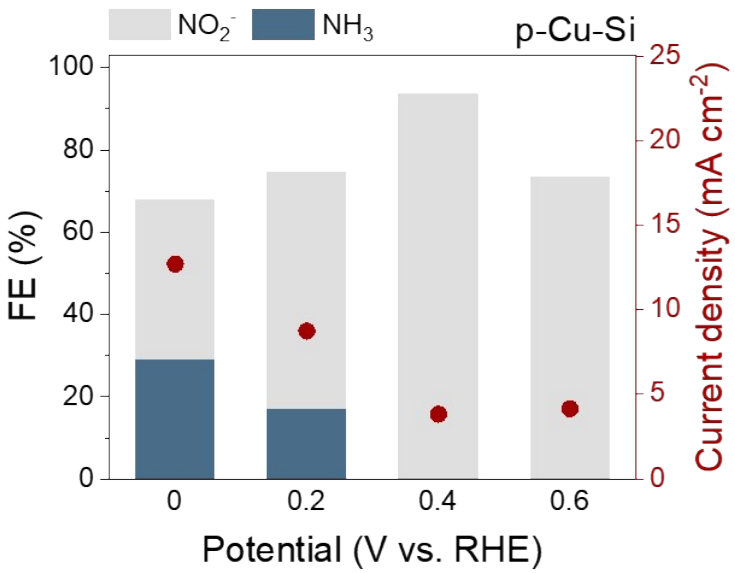

Fig. S7 Photoelectrochemical NO_3RR performance of p-Cu-Si.

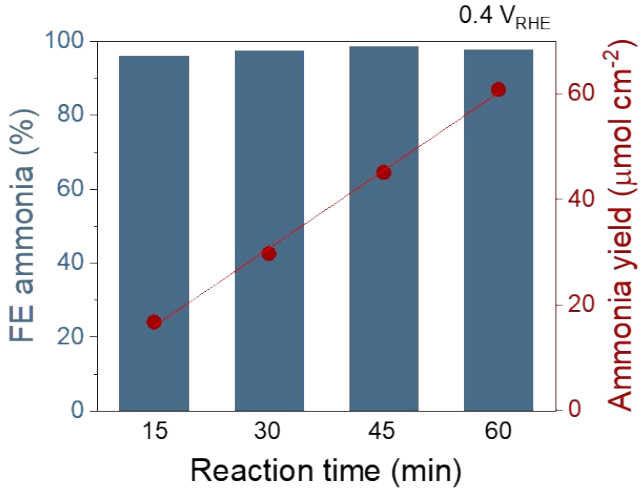

Fig. S8 Photoelectrochemical NO_3RR performance of $Cu/Co(OH)_2$-Si under different reaction times at 0.4 V_{RHE}.

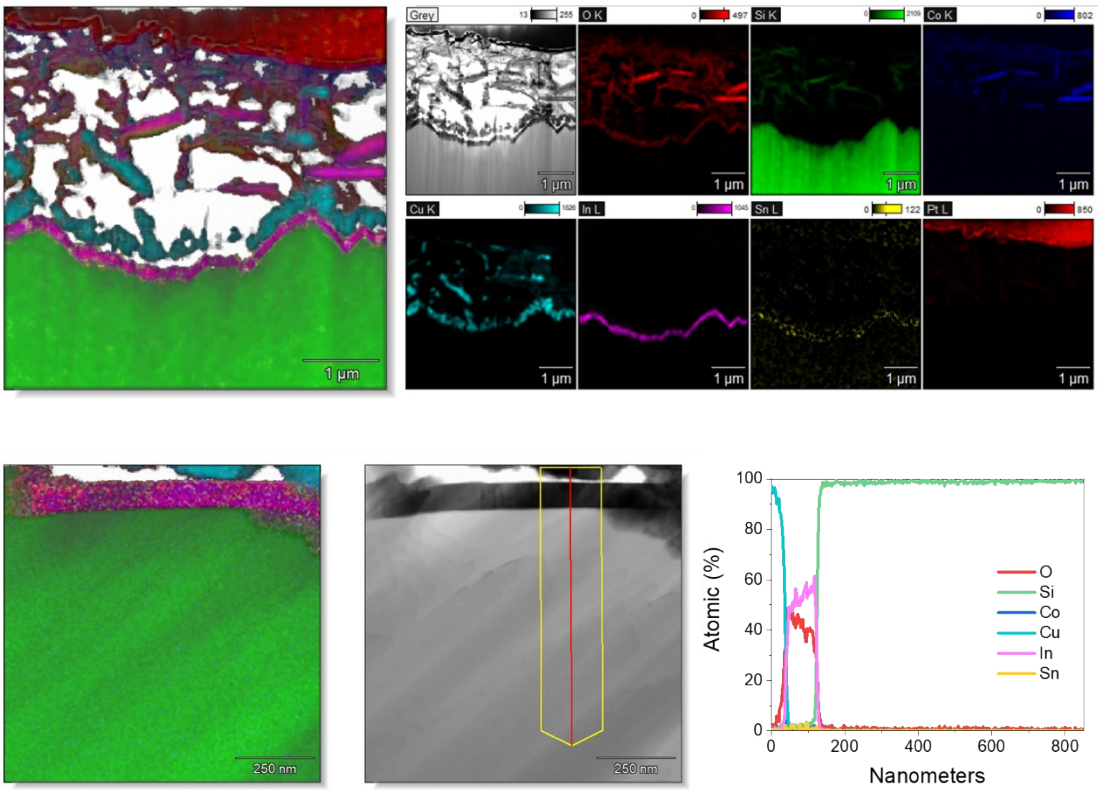

Fig. S9 Cross-sectional STEM images of spent Cu/Co(OH)$_2$-Si, corresponding EDX mapping images and linear atomic element distribution at selected region.

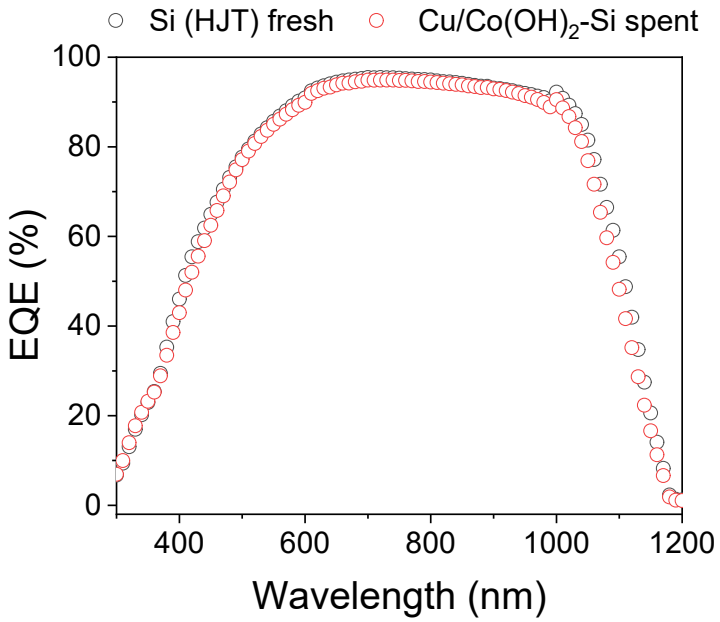

Fig. S10 EQE analysis obtained from the p-type side of fresh Si (HJT) sample and spent Cu/Co(OH)$_2$-Si.

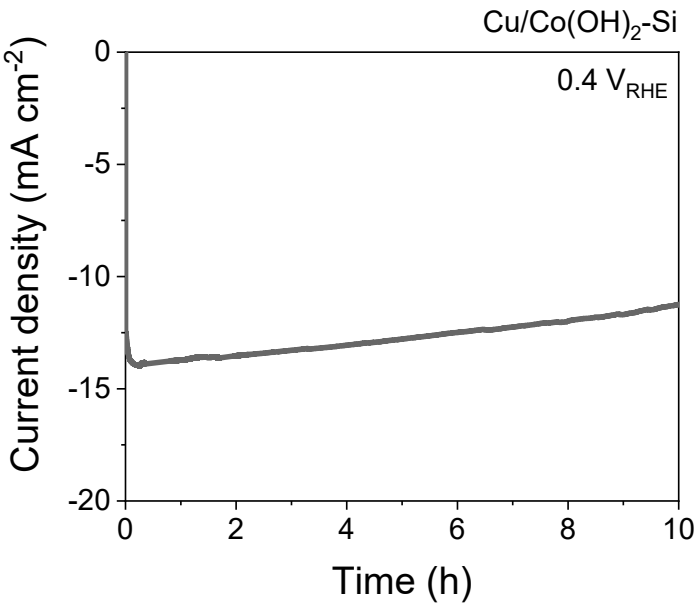

Fig. S11 10 hours stability test of $Cu/Co(OH)_2$-Si at 0.4 V_{RHE}.

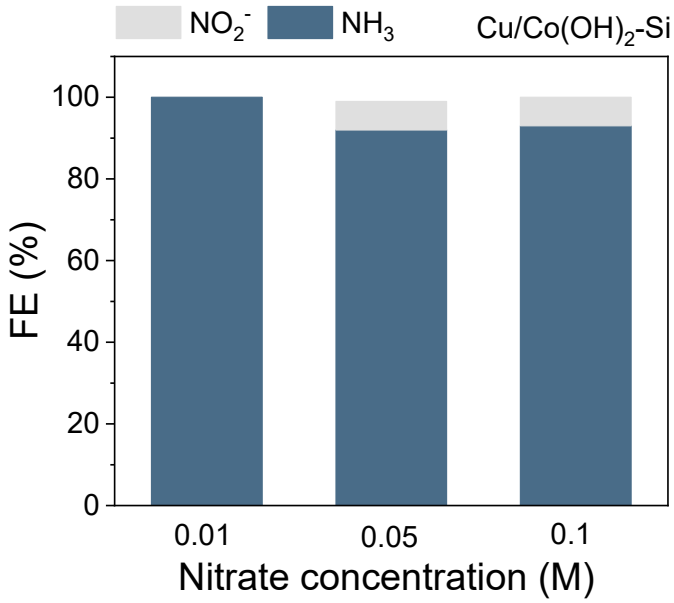

Fig. S12 The FEs of $Cu/Co(OH)_2$-Si in 0.1 M KOH containing different initial nitrate concentrations electrolyte at 0.4 V_{RHE}.

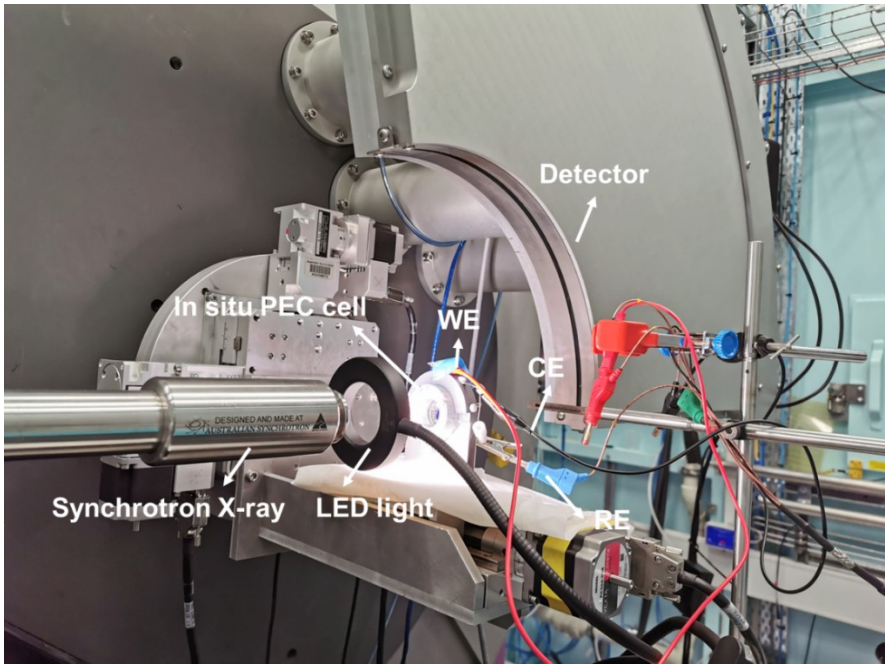

Fig. S13 Setup employed for photoelectrochemical in-situ SR-PD characterization in ANSTO, Australia.

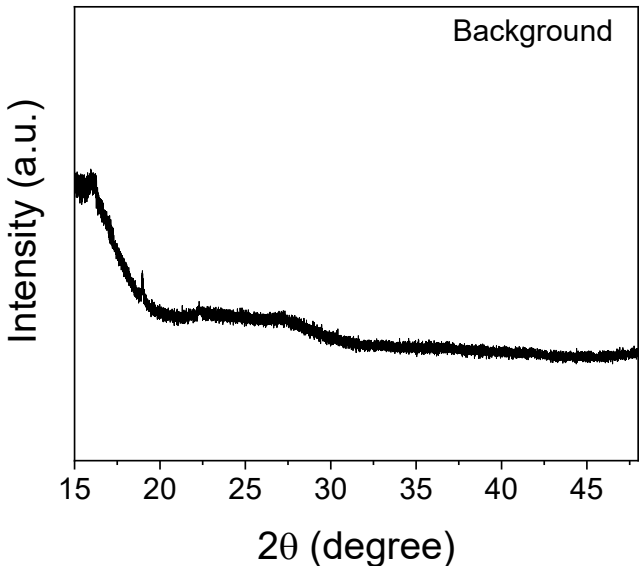

Fig. S14 PD pattern of the background.

The background is the PD pattern of Si structure in PEC cell with electrolyte and under illumination.

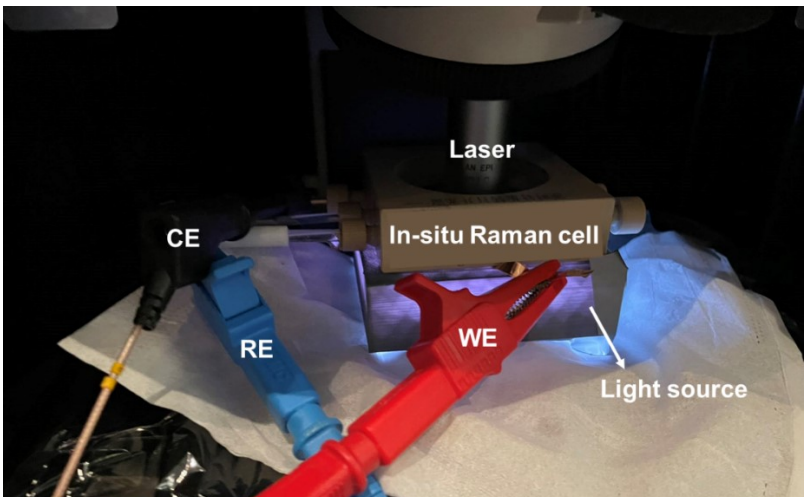

Fig. S15 Setup employed for photoelectrochemical in-situ Raman characterization.

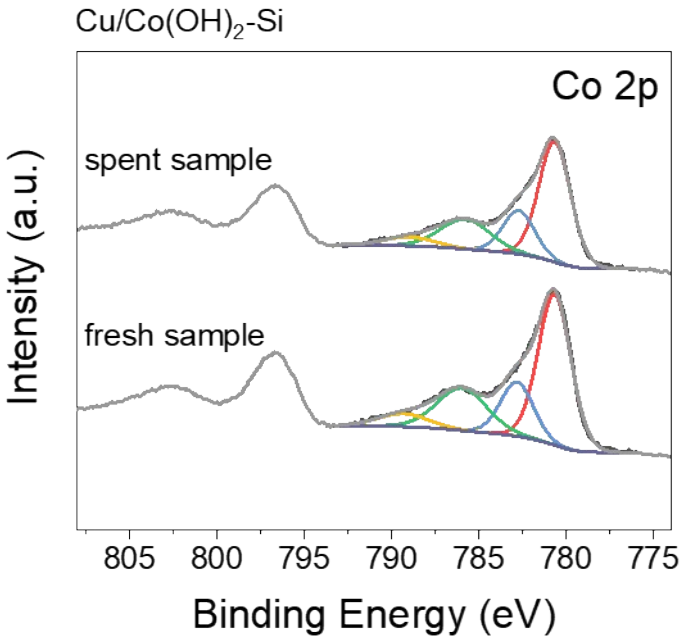

Fig. S16 XPS Co 2p spectra of fresh and spent Cu/$Co(OH)_2$-Si.

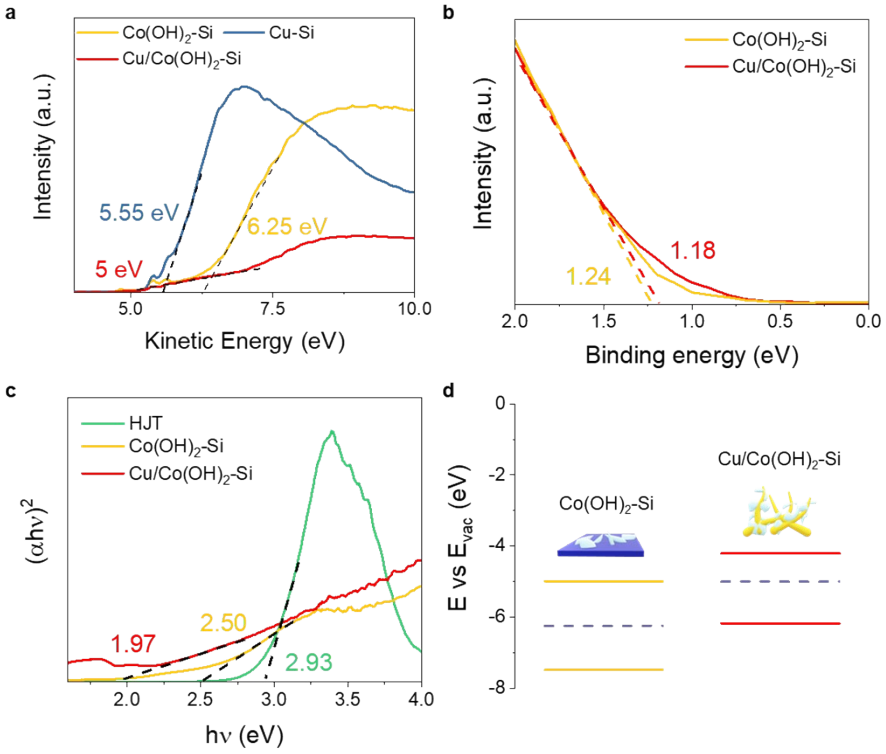

Fig. S17 (a) UPS spectra and calculated work functions. (b) VB position analysed from VB XPS spectra. (c) Tauc plots. (d) Band diagram of $Co(OH)_2$-Si and Cu/$Co(OH)_2$-Si with respect to E_{vac}.

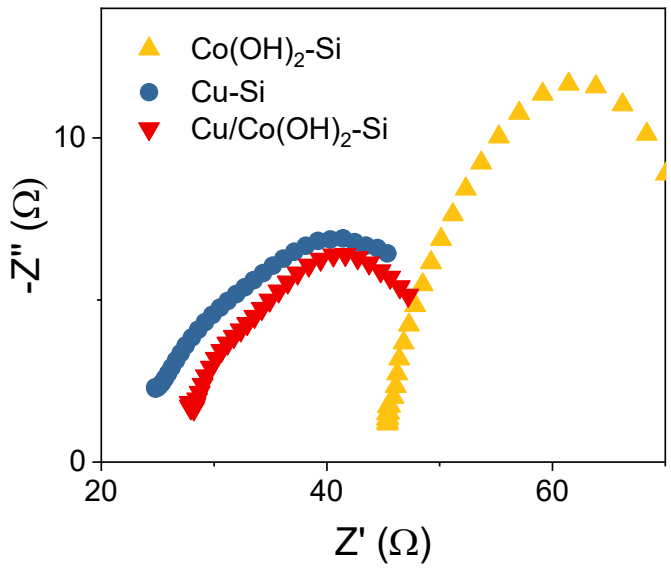

Fig. S18 EIS spectra of $Co(OH)_2$-Si, Cu-Si and Cu/$Co(OH)_2$-Si collected under illumination at 0.4 V_{RHE}.

EIS tests were performed in a frequency range of 0.01 to 10^5 Hz.

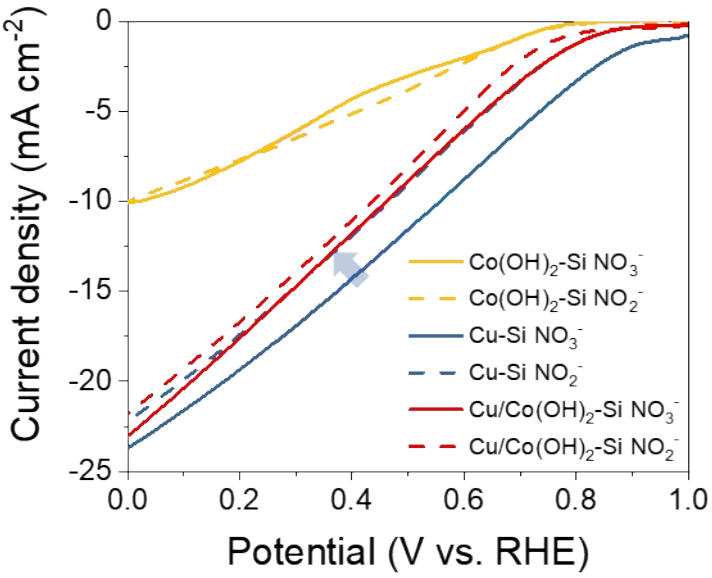

Fig. S19 LSV curves of $Co(OH)_2$-Si, Cu-Si and Cu/$Co(OH)_2$-Si collected in 0.1 M KOH+0.1 M KNO_3 or 0.1 M KOH+0.1 M KNO_2 electrolyte under photoelectrochemical test.

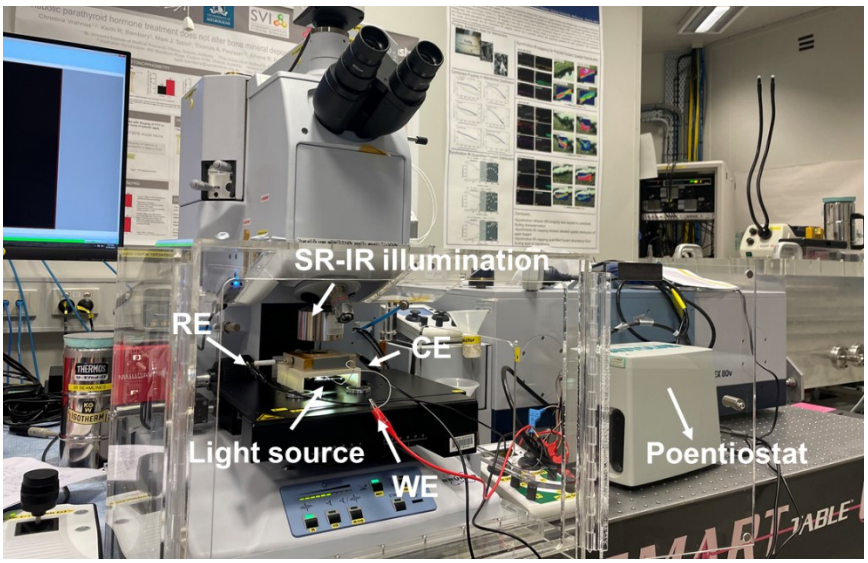

Fig. S20 Setup employed for photoelectrochemical in-situ SR-IR characterization in ANSTO, Australia.

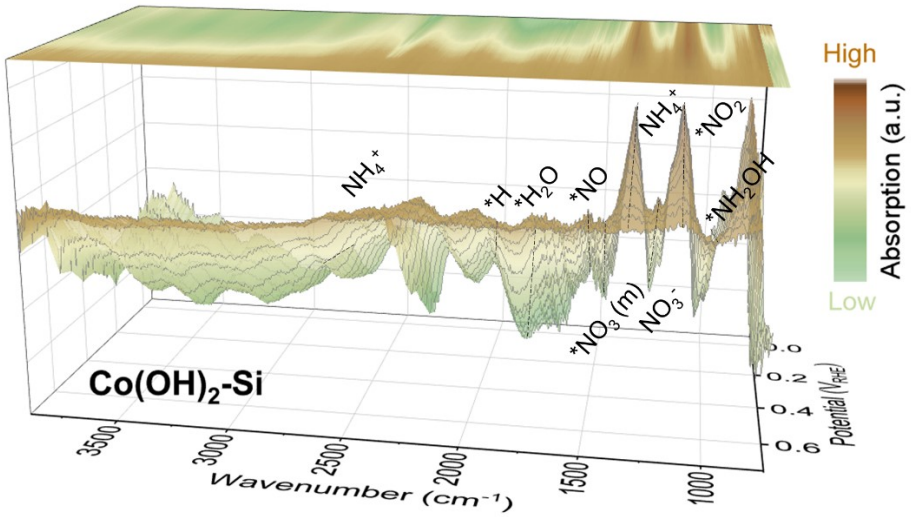

Fig. S21 Photoelectrochemical in-situ SR-IR spectra of $Co(OH)_2$-Si. Under each potential, three sets of data were collected and the time interval between each set was 2 min.

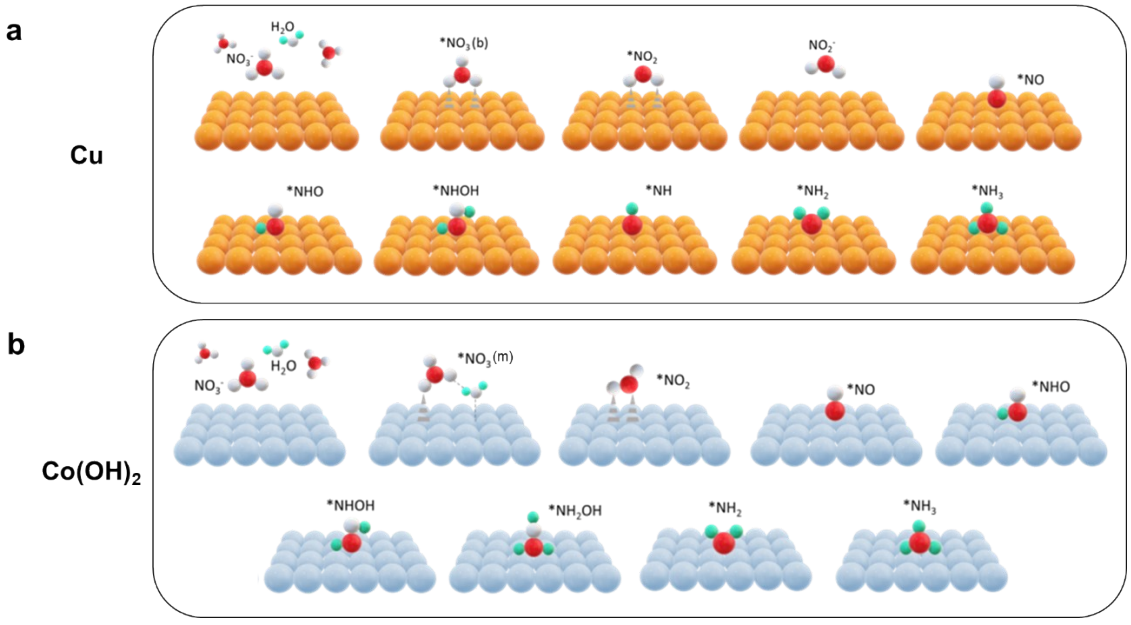

Fig. S22 Schematic diagram of reaction intermediates and adsorption configurations on (a) Cu and (b) $Co(OH)_2$.

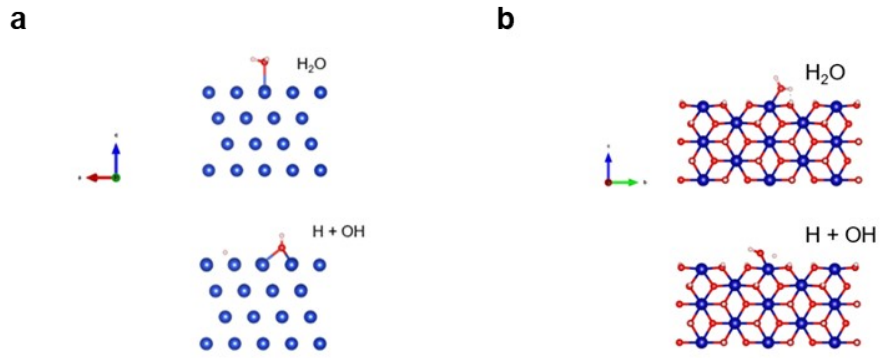

Fig. S23 The adsorption configurations of water dissociation process on (a) Cu (111) and (b) $Co(OH)_2$ (100).

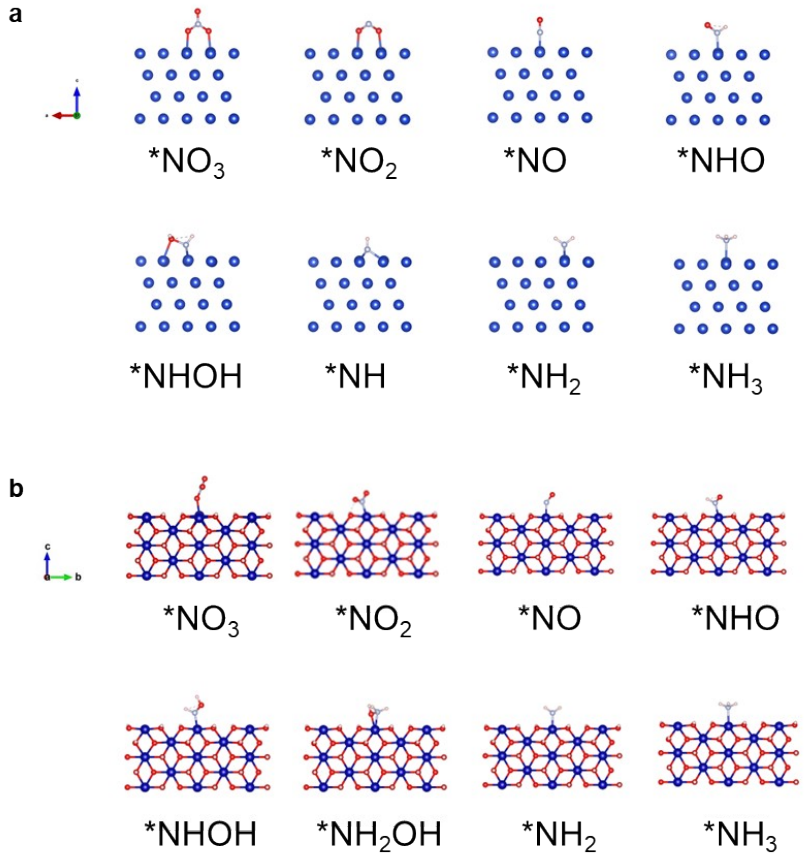

Fig. S24 Adsorption configuration of the various intermediates generated during NO_3RR on (a) Cu (111) and (b) $Co(OH)_2$ (100).

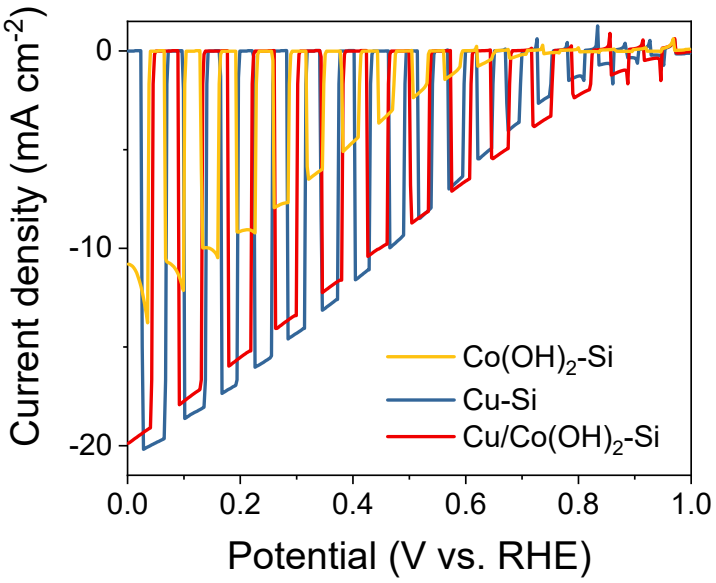

Fig. S25 LSV curves collected under chopped 1 sun illumination.

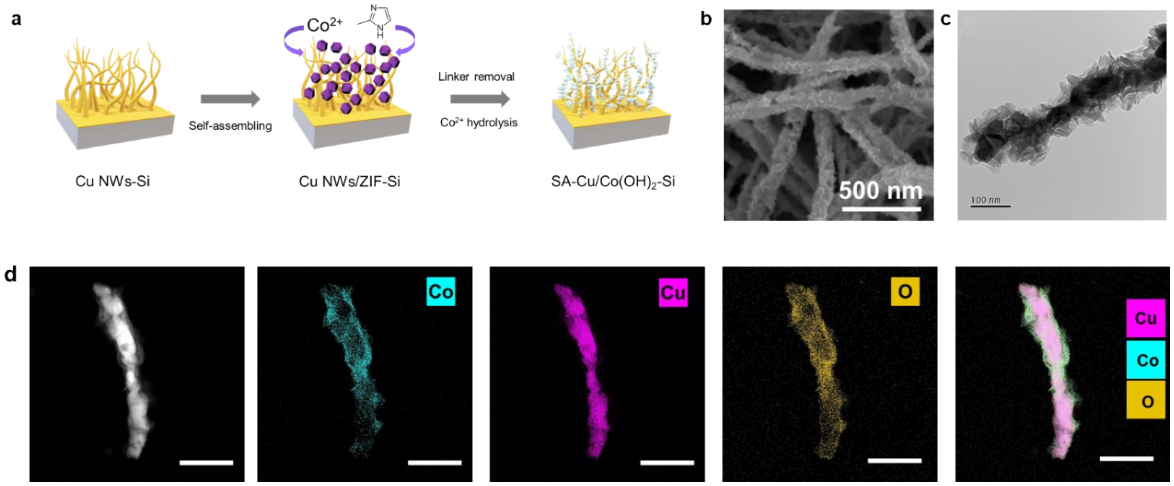

Fig. S26 (a) Schematic diagram of the facile process to produce high-efficient and large-scale SA-Cu/$Co(OH)_2$-Si. (b) SEM image, (c) TEM image, and (d) HAADF-STEM image and the corresponding elemental mapping (scale bar: 200 nm) of SA-Cu/$Co(OH)_2$-Si.

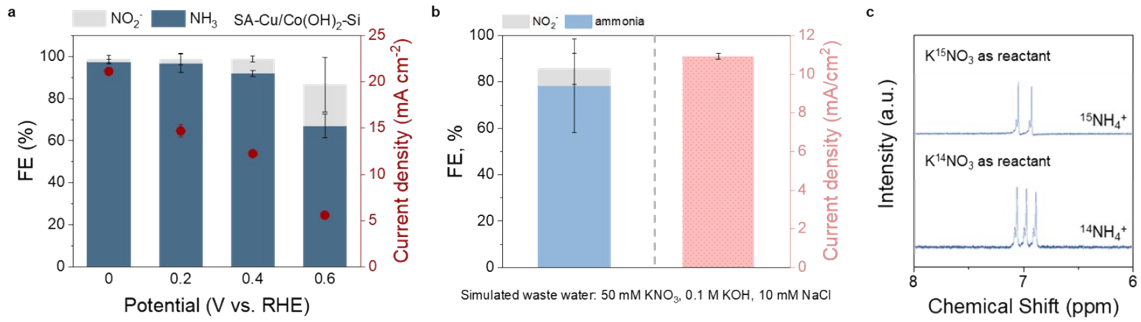

Fig. S27 (a) FE and total current density of SA-Cu/$Co(OH)_2$-Si. (b) PEC NO_3RR performance in simulated wastewater under 0.4 V_{RHE}. The simulated wastewater contains 50 mM KNO_3, 0.1 M KOH and 10 mM NaCl. (c) ^{1}H NMR spectra of the electrolyte after NO_3RR using $^{15}NO_3^-$ and $^{14}NO_3^-$ as the nitrogen source. Average values were calculated from two independent measurements, with the error bars corresponding to the standard deviation.

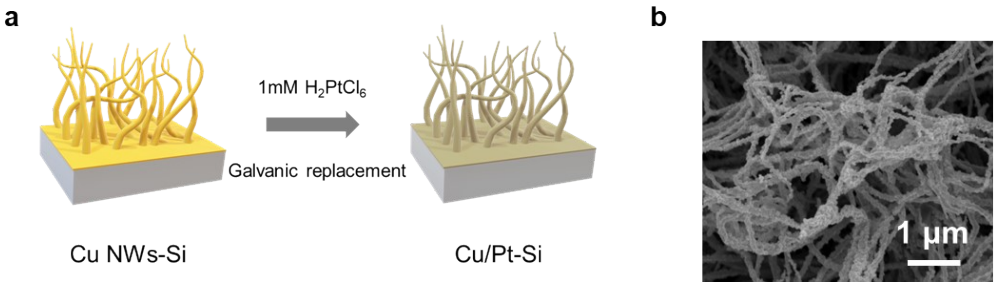

Fig. S28 (a) Schematic diagram of the facile process to produce Cu/Pt-Si. (b) SEM image of Cu/Pt-Si.

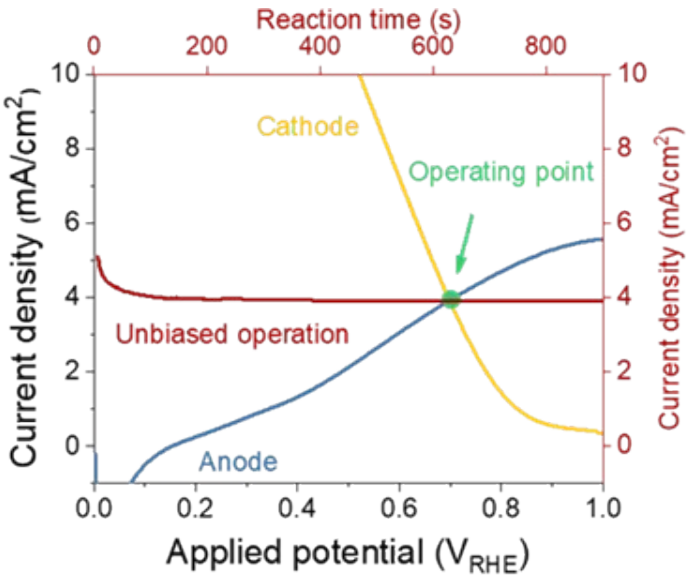

Fig. S29 LSV and chronoamperometry curves of photocathode and photoanode.

The size of photoelectrodes is 1 × 1 cm^2. The LSV curves of photocathode and photoanode were obtained in a three-electrode configuration with a Pt foil (counter) and an Ag/AgCl (reference).

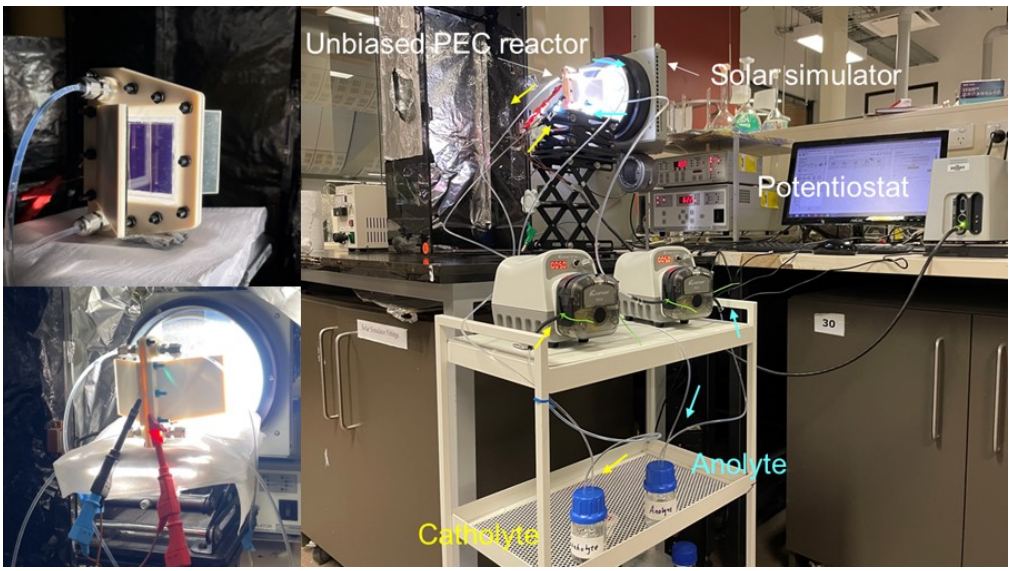

Fig. S30 Photographs of the PEC device under bias-free measurements in laboratory.

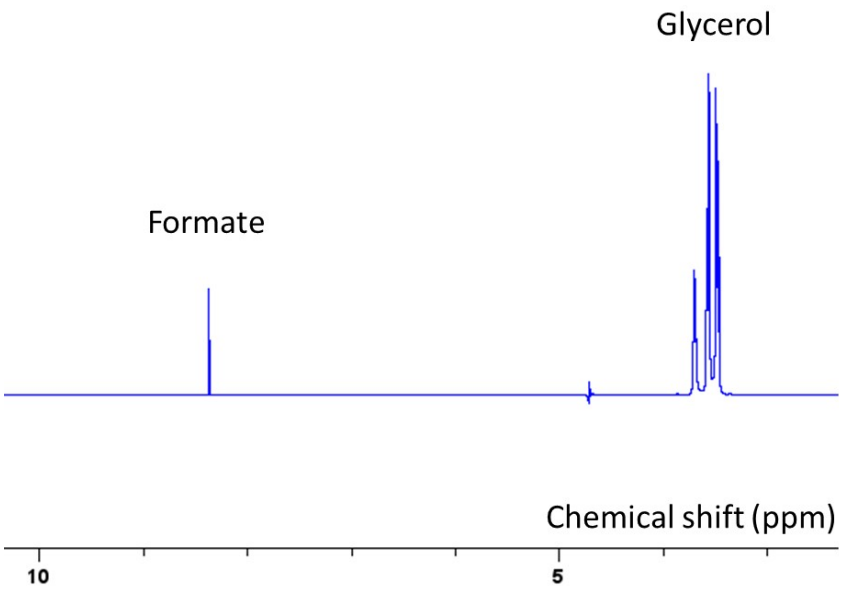

Fig. S31 ^{1}H NMR spectra of anolyte collected after laboratory bias-free testing.

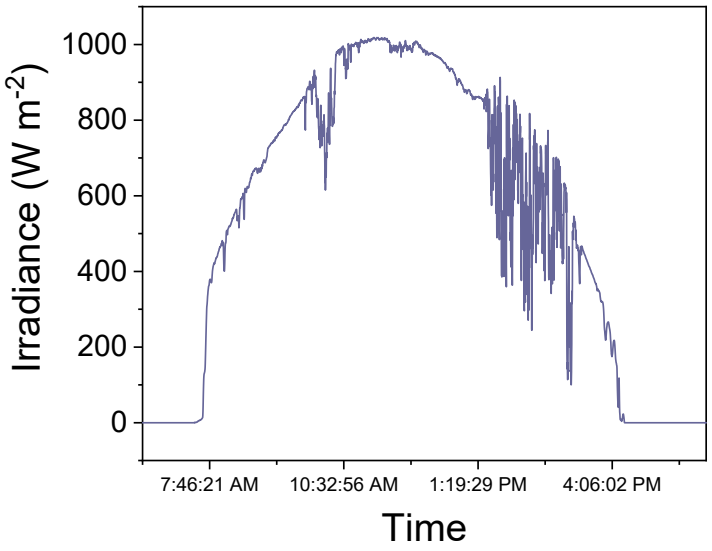

Fig. S32 The variations of solar illumination intensity on the outdoor testing day.

The outdoor tests were carried out on 10 am -2 pm, 30 May 2023.

Table S1 The performance of photoelectrodes in nitrate reduction reaction.

Sample name	Test 1						Test 2					
	V_{RHE}	FE NO_2	FE NH_3	FE H_2	Current density (mA/cm^2)	FE total	V_{RHE}	FE NO_2	FE NH_3	FE H_2	Current density (mA/cm^2)	FE total
Si	0.4	98.4	0.7	0.0	3.6	99.1	0.4	94.9	0.0	0.0	0.5	94.9
	0.2	100.0	0.0	0.0	2.9	100.0	0.2	91.4	0.0	2.0	3.5	93.4
	0.0	96.0	0.0	0.0	3.5	96.0	0.0	82.8	0.0	5.5	1.5	88.3
Cu-Si	0.6	93.0	0.5	0.0	5.5	93.5	0.6	100.0	2.0	0.0	6.5	102.0
	0.4	54.4	13.9	0.0	13.7	68.3	0.4	52.0	29.9	0.0	13.6	81.9
	0.2	50.5	27.6	0.0	16.1	78.1	0.2	67.9	24.2	0.0	14.7	92.1
	0.0	37.9	52.0	0.0	21.4	89.9	0.0	35.3	54.5	0.0	21.1	89.8
$Co(OH)_2$-Si	0.6	0.0	98.7	0.0	0.2	98.7	0.6	0.0	77.9	0.0	0.9	77.9
	0.4	0.0	99.0	0.0	2.5	99.0	0.4	0.0	95.7	0.0	4.4	95.7
	0.2	0.0	98.9	0.0	7.2	98.9	0.2	0.1	91.3	0.0	8.1	91.4
	0.0	1.2	79.8	0.0	12.1	81.0	0.0	0.9	88.4	0.0	13.3	89.3
Cu/$Co(OH)_2$-Si	0.6	7.3	92.0	0.0	3.7	99.3	0.6	5.6	90.2	0.0	6.2	95.8
	0.4	2.2	97.0	0.0	14.7	99.2	0.4	3.0	98.0	0.0	12.4	101.0
	0.2	12.0	93.5	0.0	18.8	105.5	0.2	2.0	100.0	0.0	18.4	102.0
	0.0	0.0	100.0	0.0	20.9	100.0	0.0	1.0	99.0	0.0	22.6	100.0

Table S2 Performance comparison of various photoelectrochemical and electrochemical systems on ammonia production from nitrate.

Sample name	System	Applied potential (V_{RHE})	FE_{NH3} (%)	Yield rate (μmol h^{-1} cm^{-2})	Reference
Cu/$Co(OH)_2$-HIT	PEC	0.6	91.1	22.3	This work
	PEC	0.4	97.5	65.2	This work
	PEC	0.2	96.75	88.7	This work
	PEC	0	99.5	106.6	This work
TiO_x-250/CdS/CZTS	PEC	-0.2	-	8.21	[8]
TiO_x-250/CdS/CZTS	PEC	0.1	89.1	-	[8]
O_SiNW/Au	PEC	0.2	95.6	-	[9]
O_SiNW/Au	PEC	0.1	-	0.42	[9]
CoFeMnO/$BiVO_4$	PEC	-0.1	-	1.05	[10]
Si@TiO_2-50-V_o	PEC	-0.6	94.3	63.1	[11]
$ZnIn_2S_4$/$BiVO_4$	PEC	-0.1	37.2	1.76	[12]
CuPc/CeO_2	PEC	-0.6	33	1.16	[13]
Cu/Cu_2O NWAs	EC	-0.85	95.8	244.9	[14]
O-Cu–PTCDA	EC	-0.4	85.9	25.6	[15]
Ti	EC	-1	82	-	[16]
Fe SAC	EC	-0.66	75	-	[17]
Pd/TiO_2	EC	-0.7	92.1	-	[18]

Pd/TiO_2	EC	-0.8	-	66	[18]
TiO_{2-x}	EC	-1.6 V_{SCE}	85	45	[19]
FOSP-Cu-0.1	EC	-0.266	93.91	101.4	[20]

Table S3 UPS measured work functions (W_F) (versus E_{vac}), VB XPS measured VB (versus Fermi level) and UV-Vis measured Eg.

Sample	W_F (eV)	VB (eV)	E_g (eV)
HJT			2.93
Cu-HJT	5.55		
$Co(OH)_2$-HJT	6.25	1.24	2.50
$Cu/Co(OH)_2$-HJT	5	1.18	1.97

Table S4 The assignment of Raman peaks.

Raman shift (cm^{-1})	Assignment	Reference
714	NH_3 rocking vibration	[21,22]
801	NO_2^- bending	[22]
1016	N-O stretches from the NO_2 moiety associated NO_3^-	[22,23]
1048	Symmetric NO_3^- stretch from solution nitrate	[22,23]
1183	V_s NO_2^-, chelating nitrito	[22,23]
1270	V_a NO_2^-, chelating nitrito	[22]
1307	HNH deformation of NH_3	[22]
1350	Symmetric N-O stretches from NO_2 moiety associated with absorbed NO_3^-	[22]
1385	Antisymmetric N-O stretches from NO_2 moiety associated with absorbed NO_3^-	[22]
1548	HNO stretch	[21,22]
1660	H-O-H bending	[24]

Table S5 The assignment of IR peaks.

Wavenumber (cm^{-1})	Assignment	Reference
1085	N-O stretching vibration of hydroxylamine (*NH_2OH)	25,26
1240	N-O antisymmetric stretching vibration of NO_2^-/*NO_2	25,27-29
1325	N-O antisymmetric stretching vibration of NO_3^-	25,30
1375	NH_4^+	26,27
1425	Monodentate coordination of *NO_3	30,31
1470	*NH_2 bending mode	26,32,33
1520	Vibration of adsorbed *NO in bridge mode	25,26
1638	H-O-H bending of adsorbed *H_2O	25,26
1700	Bidentate coordination of *NO_3	30
1725	N-O stretching mode of *NO	34-36
1843	Adsorbed *H on Cu site	37
1917	Adsorbed *H on $Co(OH)_2$ site	25
2805	N-H asymmetric stretching vibration of NH_4^+	38,39
3017	N-H stretching of *NH_y species	40,41
1070	*ND_2 bending mode	32
1200	*D-O-D bending of adsorbed *D_2O	42
2012	N-O stretching mode in *ND_2OD	34,43
2450	ND_4^+	44,45
2886	N-D stretching of *ND_y	46
1210	*$^{15}NO_2$	47,48
1480	$^{15}NO_3^-$	28,47,48
1619	*^{15}NO	47-49
2680	$^{15}NH_4^+$	49
2896	*^{15}NH	49
3120	*^{15}NH	49

#In isotope-labelling in-situ spectroscopy, the intermediates and products are similar, expect for the isotopic substitution.
#Deuterated bonds change their vibration frequency while non-deuterated groups reamin unaffected.

Table S6 The calculated reaction-free energies for different intermediates.

Reaction coordinate	Gibbs free energy (eV)	
	Cu (111)	$Co(OH)_2$ (100)
NO_3	0	0
$*NO_3$	-2.69	-2.81
$*NO_2$	-4.51	-5.37
NO_2	-2.49	-2.49
*NO	-5.13	-6.65
*NHO	-5.36	-6.95
*NHOH	-6.43	-6.75
$*NH_2OH$	-8.85	-5.81
*NH	-7.95	-7.28
$*NH_2$	-8.78	-8.96
$*NH_3$	-9.57	-9.51
NH_3	-8.5	-8.5

Discussion S1 Feasibility analysis

To evaluate the economic feasibility of proposed PEC technology, the techno-economic analysis has been employed.

Technical evaluation

Based on the bias-free performance test result, our device can deliver yield rates of ammonia ~0.021 mmol h^{-1} cm^{-2} (or 3.57 g h^{-1} m^{-2}) and formate ~0.078 mmol h^{-1} cm^{-2} (or 34.9 g h^{-1} m^{-2}).

The proposed PEC device is shown in Fig. SD1.

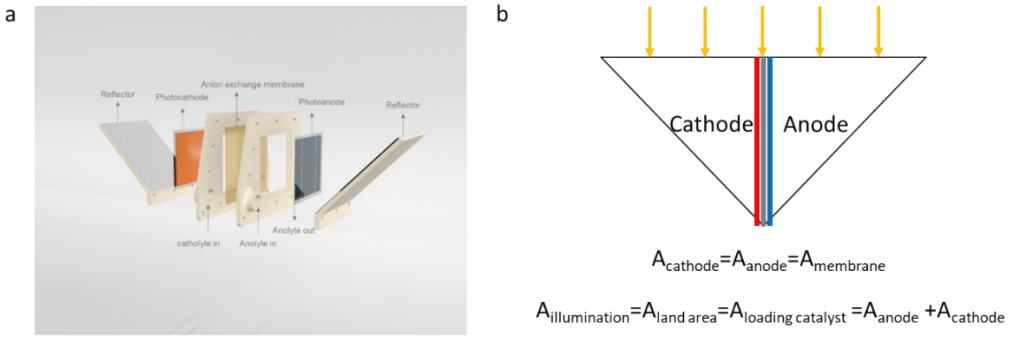

Fig. SD1 (a) Illustration of PEC device. (b) Top view of PEC device and the area relationships.

We evaluated the device from an economic standpoint. The main components in the system can be depicted in Fig. SD2.

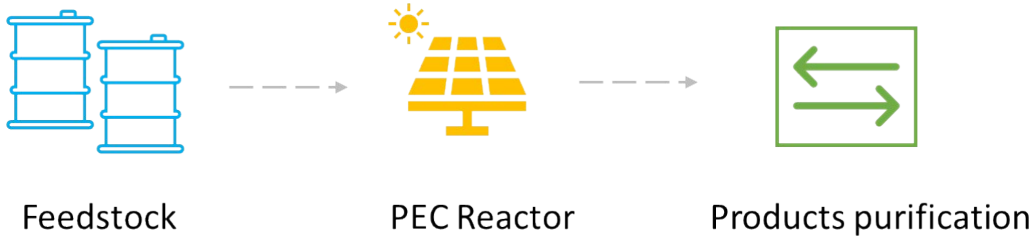

Fig. SD2 Flow diagram of primary components.

Economic analysis

Herein, an economic model has been developed to calculate the cost. The total cost can be divided into the sum of raw material, capital expenditure (CAPEX) and operation expenditure (OPEX). All currencies are denominated in USD dollar.

The value is calculated in per illumination area (m^2), while the $A_{membrane}=0.5*\ A_{illumination}$.

Table SD1 The price of raw materials

Item	Unit	Value	Ref.
Nitrate[a]	t	0 or (315)	[50]
Glycerol	t	300	[51]

a. The price of NO_x solution is referenced from literature, which considered to capture NO_x from coal-based power plants. Since there are abundant sources of nitrate-contaminated wastewater,[52] the price of NO_3^- can be regarded as free at here.

CAPEX is limited to: PEC device (Si solar cell, cocatalysts, membrane, glass, reflector, PVC cell chamber plus PEC panel assembling, support frame, PVC tubing, pump, wiring), control system, products processing device, land and installation.

OPEX is limited to: consumables replacement, maintenance, insurance and miscellaneous.

Table SD2 Summary of technical parameters and respective costs for components in CAPEX of the considered PEC system.

Item	Unit	Value	Ref.
Land	m^2	0.15	[53]
Installation	m^2	6	[54]
Si material[a]	m^2	39.95	[55]
Catalysts[b]	m^2	3.86	
Membrane[c]	m^2	25	[53]
Reflector	m^2	10	
Glass	m^2	10	[56]
PVC cell chamber plus panel assembling	m^2	20	[57]
Support frame	m^2	27	[54]
PVC tubing	m^2	6	[54]
Pump	m^2	0.003	[55]
Wiring	m^2	1.21	[55]
Control system	m^2	4	[54,57]
Products processing device	m^2	6	[56]
PV panels and land for electricity (appliance)[d]	m^2	5.01	

Others (tanks or accessories)[e]	m^2	32.8
Total	m^2	197

a. The price for Si PV panel is \$ 49.95 m^{-2}. Since considering our light-absorber is no need to assemble as the PV module and only one side needs metallisation, we assume the cost of our Si solar cell is \$ 39.95 m^{-2}.
b. Calculated assuming a combination of Cu NSTL and $Co(OH)_2$/Pt as catalyst structure. The thickness of Cu layer is around 500 nm, so the total quantity of Cu is $5x10^{-7}$ m^3 m^{-2}. Assuming the quantity of Cu will be half when produced as nanowires, the total Cu quantity in our case is $2.5*10^{-7}$ m^3 m^{-2}, with weight 22.35 g m^{-2}. Since the Cu price is \$8.21 per kg, the Cu cost is \$ 0.183 m^{-2}. Similarly, assuming the thickness of $Co(OH)_2$ and Pt are 50 nm and 10 nm, respectively, the price of them are \$ 0.0054 m^{-2} and 7.35 m^{-2}, respectively.
c. The $A_{membrane}$ is the half of $A_{illumination}$. So the membrane price is half of \$50.
d. Calculated assuming the area of solar panels providing electricity to control system, pump and other appliance is 10% area of photoelectrodes. The solar panel and associated land cost is \$ 5.01 m^{-2}.
e. Considering the cost in others is 20% of total CAPEX.

Table SD3 Summary of items and costs of OPEX in the considered PEC system (for 20 years).

Item	Unit	Value	Ref.
Catalyst replacement	m^2	34.74	Each 2 years
Membrane replacement	m^2	25	Each 10 years
Maintenance (5% of CAPEX)	m^2	9.85	[54]
Insurance (2% of CAPEX)	m^2	3.94	[56]
Miscellaneous (5% of OPEX)	m^2	3.67	[57]
Total	m^2	77.2	

Application scenarios

There are two scenarios have been considered: one is the on-site fertilizer device for agriculture application and the other one is the industrial plant for stand-alone ammonia production.

In Australia, the average peak sun hour is around 3.8 to 6.3 per day. Hence, we assume the solar irradiation time for PEC production is 5 hours per day.[57,58]

The cathodic product contains NH_4^+, K^+ and NO_3^-, which can further capture CO_2 to produce fertilizer directly.[59] The anodic product formate can be purified to obtain formic acid, which can be used in multiple ways: (i) as energy or hydrogen carrier in fuel cells, (ii) as preservative and antibacterial agent in livestock feed, (iii) used in other manufacturing processes.

Table SD4 The price of products

Item	Unit	Value	Ref.
Ammonia	t	1000	[60]
Formic acid	t	1200	[59]

An on-site fertilizer device:

In the world, the average nitrogen fertilizer use (in kilograms of nitrogen per hectare, 10000 m^2) of cropland is ~ 72 kg (Australia 43.15 kg) in 2020. The area of independent PEC system can be calculated as follows:

$$Area\ of\ photocathode = \frac{Amout\ of\ NH_3\ produced\ per\ day\ (g)}{Solar\ irradiation\ time\ (h) \times NH_3\ yield\ (g \cdot m^{-2} \cdot h^{-1})} = \frac{}{5\ (h)}$$
$$= 13.42\ m^2$$

Since we employed a dual-reflector flow reactor, the illumination area (land area) should be the sum of photocathode and photoanode. Therefore, to fertilize 10000 m^2 cropland, a 26.8 m^2 PEC system is required. In Australia, the required PEC system can be reduced to 16.1 m^2.

Therefore, the production rate of our current single PEC device can satisfy the requirements of 1.49 m^2 cropland.

To fertilize 10000 m^2 cropland in 20 years with a 26.8 m^2 PEC system, the total cost is $ 7348, which is similar with the price of purchasing commercial fertilizers $ 7200 (240 kg fertilizer per year, \$1.5 kg^{-1}, 20 years).

For the fertilizer purpose, the conversion of nitrate to ammonia has two key reasons. One reason is that ammonium would be more stable in soil than nitrate. The other reason is that by combing the nitrate-ammonia process with other reactions, such as CO_2 reduction, other types of fertilizer like urea can also be further produced.[61]

The on-site PEC system produced ammonia will be diluted in intelligent irrigation systems and employed in green and sustainable agriculture.

A plant for NH_3 production:

Assuming the NH_3 production rate of PEC plant is 1 t per day and the corresponding formate production rate is 9.78 t per day. The plant lifetime is 20 years. The replacement of catalyst is assumed as re-deposit catalysts on previous Si substrate.

Table SD5 Summary of the assumptions required in PEC system analysis.

Parameter	Unit	Value	Reference
Ammonia production rate	t/day	1	
Formate production rate	t/day	9.78	
Economic lifetime	Years	20	[55,57]
Catalyst replacement	Years	2	[57]
Membrane replacement	Year	10	[55]

Similarly,

$$Area\ of\ photocathode = \frac{Amout\ of\ NH_3\ produced\ per\ day\ (g)}{Solar\ irradiation\ time\ (h) \times NH_3\ yield\ (g \cdot m^{-2} \cdot h^{-1})} = \frac{}{5\ (h)}$$
$$= 56022\ m^2$$

The area under illumination (or land area) is 112044.8 m^2. (This area is equal to 15.69 standard football pitches.)

In 20 years, the CAPEX is \$ 2.2 $\times 10^7$ and the operation fee is \$ 8.6 $\times 10^6$. The plant can produce ammonia and formate 7300 t and 71394 t, respectively.

Hence, the cost on per day is ((CAPEX +OPEX) /7300 days) + cost of raw material = ((197+77.2) × 112044.8 ÷ 7300) + 3.65 × 0+ 7.85 × 300 = 4208.6+2354.1=$6562.7.

The associated products revenue is 1 × 1000 + 9.78 × 1200 = $12736.

The profit of per day is $6173, which indicates the PEC system has economic feasibility.

The result emphasized on the importance of using the anode side to produce high value co-products. Compared with OER, GOR not only boosts the reaction efficiency, but also improves the economic benefits.

Product engineering

To produce pure ammonia from the reduction of N-containing waste, several possible strategies exist. Firstly, methods such as cool condensation, electrochemical separation, and selective deionization can be used to enrich and separate the produced ammonia to form pure products.[62] Secondly, using a high concentration of nitrate as the reactant would be advantageous, especially when the system is further heated, as this would facilitate ammonia gas formation. In this process, utilizing thermal energy from solar sources appears attractive.[63] Thirdly, using gas-phase N-containing wastes, such as NO and N_2O, can produce ammonia gas directly.[64]

The produced ammonium can be converted into other ammonium salts, such as NH_4Cl via an acid trap and NH_4HCO_3 via a CO_2 trap.[62] These ammonium salts have wide applications in many industrial fields.

Additionally, the nitrate reduction system can be assembled as a Zn-NO_3^- battery to work as an energy-output electrocatalytic system.[65]

Sensitive analysis

Table SD6 System parameters for low-, base-, and high-case scenarios used in the sensitive analysis.

Parameter	low	base	high
Catalysts price ($)	0.183[a]	3.86	73.5[b]
PV material price ($)	15.98[c]	39.95	400[d]
Performance ($gNH_3\ h^{-1}\ m^{-2}$)	17.85[e]	3.57	0.714[f]
Plant lifetime	30	20	10
Catalyst reuse	5	2	1
Membrane reuse	20	10	5

Daylight hours	7	5	3

a. Considering using Cu as catalyst in both cathode and anode.
b. Considering using 100 nm Pt on Cu-NSTL in photoanode.
c. Considering using Si+Perovskite, the price is 40% of Si.[55]
d. Considering using more expensive materials, such as III-V materials, which has been widely used in current PV-EC research.[66,67]
e. Considering the performance is fivefold higher than the current one.
f. Considering the performance is one fifth of the current one.

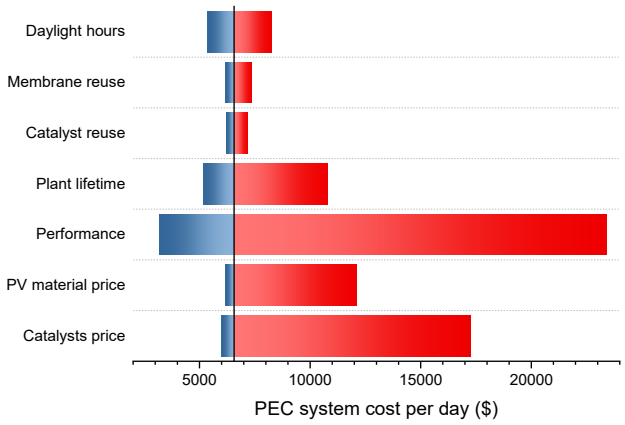

Fig. SD3 Sensitivity analysis of PEC system cost per day. Blue represents optimistic (low cost) estimates, and red represents pessimistic (high cost) estimates.

The production cost is very sensitive to PEC performance, solar cell price and catalyst price. Hence, our work with using cost-effective commercial Si solar cell and non-precious catalysts to achieve high performance is a good demonstration for the rational design of PEC system.

Environmental impacts

The PEC system will be powered by solar energy and produce NH_3 in a clean process with negligible carbon emissions. The product purification process will further capture and use CO_2.

Comparing with conventional Haber-Bosch process, the PEC system can save fossil fuel energy around 30 GJ and reduce CO_2 emissions 2.16 t when produce per ton NH_3.[68]

References

1 Zhang, B. *et al.* Defect-rich 2D material networks for advanced oxygen evolution catalysts. *ACS Energy Lett.* **4**, 328-336, doi:https://doi.org/10.1021/acsenergylett.8b02343 (2018).

2 Kresse, G. & Furthmüller, J. Efficiency of ab-initio total energy calculations for metals and semiconductors using a plane-wave basis set. *Comput. Mater. Sci.* **6**, 15-50, doi:https://doi.org/10.1016/0927-0256(96)00008-0 (1996).

3 Kresse, G. & Furthmüller, J. Efficient iterative schemes for ab initio total-energy calculations using a plane-wave basis set. *Phys. Rev. B* **54**, 11169, doi: https://doi.org/10.1103/PhysRevB.54.11169 (1996).

4 Blöchl, P. E. Projector augmented-wave method. *Phys. Rev. B* **50**, 17953, doi: https://doi.org/10.1103/PhysRevB.50.17953 (1994).

5 Kresse, G. & Joubert, D. From ultrasoft pseudopotentials to the projector augmented-wave method. *Phys. Rev. B* **59**, 1758, doi: https://doi.org/10.1103/PhysRevB.59.1758 (1999).

6 Perdew, J. P., Burke, K. & Ernzerhof, M. Generalized gradient approximation made simple. *Phys. Rev. Lett.* **77**, 3865, doi: https://doi.org/10.1103/PhysRevLett.77.3865 (1996).

7 Grimme, S., Antony, J., Ehrlich, S. & Krieg, H. A consistent and accurate ab initio parametrization of density functional dispersion correction (DFT-D) for the 94 elements H-Pu. *J. Chem. Phys* **132**, 154104, doi: https://doi.org/10.1063/1.3382344 (2010).

8 Zhou, S. *et al.* Engineering a kesterite-based photocathode for photoelectrochemical ammonia synthesis from NO_x reduction. *Adv. Mater.* **34**, 2201670, doi:https://doi.org/10.1002/adma.202201670 (2022).

9 Kim, H. E. *et al.* Photoelectrochemical nitrate reduction to ammonia on ordered silicon nanowire array photocathodes. *Angew. Chem. Int. Ed.* **61**, e202204117, doi:https://doi.org/10.1002/anie.202204117 (2022).

10 Wang, F. *et al.* Fabrication of an amorphous metal oxide/p-$BiVO_4$ photocathode: understanding the role of entropy for reducing nitrate to ammonia. *Inorg. Chem. Front.* **9**, 805-813, doi:10.1039/D1QI01472B (2022).

11 Xu, M. *et al.* Atomic layer deposition technique refining oxygen vacancies in TiO_2 passivation layer for photoelectrochemical ammonia synthesis. *Compos. Commun.* **29**, 101037, doi:https://doi.org/10.1016/j.coco.2021.101037 (2022).

12 Wang, F. *et al.* Frustrated Lewis pairs boosting photoelectrochemical nitrate reduction over $ZnIn_2S_4/BiVO_4$ heterostructure. *Chem. Eng. J.* **450**, 138260, doi:https://doi.org/10.1016/j.cej.2022.138260 (2022).

13 Li, X. *et al.* Photoelectrochemical reduction of nitrate to ammonia over $CuPc/CeO_2$ heterostructure: Understanding the synergistic effect between oxygen vacancies and Ce sites. *Chem. Eng. J.* **433**, 133225, doi:https://doi.org/10.1016/j.cej.2021.133225 (2022).

14 Wang, Y., Zhou, W., Jia, R., Yu, Y. & Zhang, B. Unveiling the activity origin of a copper-based electrocatalyst for selective nitrate reduction to ammonia. *Angew. Chem. Int. Ed.* **59**, 5350-5354, doi:https://doi.org/10.1002/anie.201915992 (2020).

15 Chen, G.-F. *et al.* Electrochemical reduction of nitrate to ammonia via direct eight-electron transfer using a copper–molecular solid catalyst. *Nat. Energy* **5**, 605-613, doi:10.1038/s41560-020-0654-1 (2020).

16 McEnaney, J. M. *et al.* Electrolyte engineering for efficient electrochemical nitrate reduction to ammonia on a titanium electrode. *ACS Sustain. Chem. Eng.* **8**, 2672-2681, doi:10.1021/acssuschemeng.9b05983 (2020).

17 Wu, Z.-Y. *et al.* Electrochemical ammonia synthesis via nitrate reduction on Fe single atom catalyst. *Nat. Commun.* **12**, 2870, doi:10.1038/s41467-021-23115-x (2021).

18 Guo, Y. *et al.* Pd doping-weakened intermediate adsorption to promote electrocatalytic nitrate reduction on TiO_2 nanoarrays for ammonia production and energy supply with zinc–nitrate batteries. *Energy Environ. Sci.* **14**, 3938-3944, doi:10.1039/D1EE00806D (2021).

19 Jia, R. *et al.* Boosting selective nitrate electroreduction to ammonium by constructing oxygen vacancies in TiO_2. *ACS Catal.* **10**, 3533-3540, doi:10.1021/acscatal.9b05260 (2020).

20 Zhao, Y. *et al.* Flower-like open-structured polycrystalline copper with synergistic multi-crystal plane for efficient electrocatalytic reduction of nitrate to ammonia. *Nano Energy* **97**, 107124, doi:https://doi.org/10.1016/j.nanoen.2022.107124 (2022).

21 Lei, F. *et al.* Electrochemical reduction of nitrate on silver surface and an in situ Raman spectroscopy study. *Inorg. Chem. Front.* **9**, 2734-2740, doi:10.1039/D2QI00489E (2022).

22 Butcher, D. P. & Gewirth, A. A. Nitrate reduction pathways on Cu single crystal surfaces: Effect of oxide and Cl^-. *Nano Energy* **29**, 457-465, doi:https://doi.org/10.1016/j.nanoen.2016.06.024 (2016).

23 Gao, W. *et al.* Alloying of Cu with Ru enabling the relay catalysis for reduction of nitrate to ammonia. *Adv. Mater.* **35**, 2202952, doi:https://doi.org/10.1002/adma.202202952.

24 Wang, Y.-H. *et al.* In situ electrochemical Raman spectroscopy and ab initio molecular dynamics study of interfacial water on a single-crystal surface. *Nat. Protoc.* **18**, 883-901, doi:10.1038/s41596-022-00782-8 (2023).

25 Fang, J.-Y. *et al.* Ampere-level current density ammonia electrochemical synthesis using CuCo nanosheets simulating nitrite reductase bifunctional nature. *Nat. Commun.* **13**, 7899, doi:10.1038/s41467-022-35533-6 (2022).

26 Chen, K. *et al.* p-Block antimony single-atom catalysts for nitric oxide electroreduction to ammonia. *ACS Energy Lett.* **8**, 1281-1288, doi:10.1021/acsenergylett.2c02882 (2023).

27 Pérez-Gallent, E., Figueiredo, M. C., Katsounaros, I. & Koper, M. T. M. Electrocatalytic reduction of nitrate on copper single crystals in acidic and alkaline solutions. *Electrochim. Acta* **227**, 77-84, doi:https://doi.org/10.1016/j.electacta.2016.12.147 (2017).

28 Mikhaylov, R. V. *et al.* FTIR and TPD study of the room temperature interaction of a NO–oxygen mixture and of NO_2 with titanium dioxide. *J. Phys. Chem. C* **117**, 10345-10352, doi:10.1021/jp311593s (2013).

29 Da Cunha, M., Weber, M. & Nart, F. C. On the adsorption and reduction of NO_3^- ions at Au and Pt electrodes studied by in situ FTIR spectroscopy. *J. Electroanal. Chem.* **414**, 163-170, doi:https://doi.org/10.1016/0022-0728(96)04697-9 (1996).

30 Mihaylov, M. Y. *et al.* Infrared spectra of surface nitrates: Revision of the current opinions based on the case study of ceria. *J. Catal.* **394**, 245-258, doi:https://doi.org/10.1016/j.jcat.2020.06.015 (2021).

31 Sá, J. & Anderson, J. A. FTIR study of aqueous nitrate reduction over Pd/TiO_2. *Appl. Catal. B* **77**, 409-417, doi:https://doi.org/10.1016/j.apcatb.2007.08.013 (2008).

32 Rosca, V., Beltramo, G. L. & Koper, M. T. M. Hydroxylamine electrochemistry at polycrystalline platinum in acidic media: a voltammetric, DEMS and FTIR study. *J. Electroanal. Chem.* **566**, 53-62, doi:https://doi.org/10.1016/j.jelechem.2003.11.011 (2004).

33 Yao, Y., Zhu, S., Wang, H., Li, H. & Shao, M. A Spectroscopic study on the nitrogen electrochemical reduction reaction on gold and platinum surfaces. *J. Am. Chem. Soc.* **140**, 1496-1501, doi:10.1021/jacs.7b12101 (2018).

34 Souza-Garcia, J., Ticianelli, E. A., Climent, V. & Feliu, J. M. Mechanistic changes observed in heavy water for nitrate reduction reaction on palladium-modified Pt(hkl) electrodes. *Chem. Sci.* **3**, 3063-3070, doi:10.1039/C2SC20490H (2012).

35 Rodes, A., Gómez, R., Pérez, J. M., Feliu, J. M. & Aldaz, A. On the voltammetric and spectroscopic characterization of nitric oxide adlayers formed from nitrous acid on Pt(h,k,l) and Rh(h,k,l) electrodes. *Electrochim. Acta* **41**, 729-745, doi:https://doi.org/10.1016/0013-4686(95)00362-2 (1996).

36 Rodes, A. *et al.* In situ FTIR spectroscopy characterization of the NO adlayers formed at platinum single crystal electrodes in contact with acidic solutions of nitrite. *Langmuir* **11**, 3549-3553, doi:10.1021/la00009a043 (1995).

37 Razaghianpour, M., Hantehzadeh, M. R., Sari, A. H. & Darabi, E. Electric field assisted-laser ablation of cu nanoparticles in ethanol and investigation of their properties. *Opt. Quantum Electron.* **54**, 23, doi:10.1007/s11082-021-03286-z (2021).

38 Gong, Z. *et al.* Regulating surface oxygen species on copper (I) oxides via plasma treatment for effective reduction of nitrate to ammonia. *Appl. Catal. B* **305**, 121021, doi:https://doi.org/10.1016/j.apcatb.2021.121021 (2022).

39 Wu, H. B., Chan, M. N. & Chan, C. K. FTIR characterization of polymorphic transformation of ammonium nitrate. *Aerosol Sci. Technol.* **41**, 581-588, doi: https://doi.org/10.1080/02786820701272038 (2007).

40 Fan, K. *et al.* Active hydrogen boosts electrochemical nitrate reduction to ammonia. *Nat. Commun.* **13**, 7958, doi:10.1038/s41467-022-35664-w (2022).

41 Zhang, N. *et al.* Governing interlayer strain in bismuth nanocrystals for efficient ammonia electrosynthesis from nitrate reduction. *ACS Nano* **16**, 4795-4804, doi:10.1021/acsnano.2c00101 (2022).

42 Artemov, V. G. *et al.* Revealing excess protons in the infrared spectrum of liquid water. *Sci. Rep.* **10**, 11320, doi:10.1038/s41598-020-68116-w (2020).

43 Nightingale, R. E. & Wagner, E. L. The vibrational spectra and structure of solid hydroxylamine and deutero-hydroxylamine. *J. Chem. Phys.* **22**, 203-208, doi:10.1063/1.1740030 (1954).

44 Holt, J. S., Sadoskas, D. & Pursell, C. J. Infrared spectroscopy of the solid phases of ammonia. *J. Chem. Phys.* **120**, 7153-7157, doi: https://doi.org/10.1063/1.1669380 (2004).

45 Süzer, S. & Andrews, L. FTIR spectra of ammonia clusters in noble gas matrices. *J. Chem. Phys.* **87**, 5131-5140, doi: https://doi.org/10.1063/1.453681 (1987).

46 Liu, H., Wang, Y. & Bowman, J. M. Quantum local monomer IR spectrum of liquid D_2O at 300 K from 0 to 4000 cm^{-1} Is in near-quantitative agreement with experiment. *J. Phys. Chem. B* **120**, 2824-2828, doi:10.1021/acs.jpcb.6b01722 (2016).

47 Mihaylov, M. Y., Ivanova, E. Z., Vayssilov, G. N. & Hadjiivanov, K. I. Revisiting ceria-NO_x interaction: FTIR studies. *Catal. Today* **357**, 613-620, doi:https://doi.org/10.1016/j.cattod.2019.05.014 (2020).

48 Mihaylov, M. Y. *et al.* Species formed during NO adsorption and $NO + O_2$ co-adsorption on ceria: A combined FTIR and DFT study. *Mol. Catal.* **451**, 114-124, doi:https://doi.org/10.1016/j.mcat.2017.11.030 (2018).

49 Han, S. et al. Ultralow overpotential nitrate reduction to ammonia via a three-step relay mechanism. *Nat. Catal.*, **6**, 402-414, doi:10.1038/s41929-023-00951-2 (2023).

50 Daiyan, R. *et al.* Nitrate reduction to ammonium: from CuO defect engineering to waste NO_x-to-NH_3 economic feasibility. *Energy Environ. Sci.* **14**, 3588-3598, doi:10.1039/D1EE00594D (2021).

51 Oh, L. S. *et al.* How to change the reaction chemistry on nonprecious metal oxide nanostructure materials for electrocatalytic oxidation of biomass-derived glycerol to renewable chemicals. *Adv. Mater.* **35**, 2203285, doi:https://doi.org/10.1002/adma.202203285 (2023).

52 van Langevelde, P. H., Katsounaros, I. & Koper, M. T. M. Electrocatalytic nitrate reduction for sustainable ammonia production. *Joule* **5**, 290-294, doi:https://doi.org/10.1016/j.joule.2020.12.025 (2021).

53 Grimm, A., de Jong, W. A. & Kramer, G. J. Renewable hydrogen production: A techno-economic comparison of photoelectrochemical cells and photovoltaic-electrolysis. *Int. J. Hydrog. Energy* **45**, 22545-22555, doi:https://doi.org/10.1016/j.ijhydene.2020.06.092 (2020).

54 Uekert, T., Pichler, C. M., Schubert, T. & Reisner, E. Solar-driven reforming of solid waste for a sustainable future. *Nat. Sustain.* **4**, 383-391, doi:10.1038/s41893-020-00650-x (2021).

55 Wang, Y. *et al.* Direct solar hydrogen generation at 20% efficiency using low-cost materials. *Adv. Energy Mater.* **11**, 2101053, doi:https://doi.org/10.1002/aenm.202101053 (2021).

56 Wenderich, K. *et al.* Industrial feasibility of anodic hydrogen peroxide production through photoelectrochemical water splitting: a techno-economic analysis. *Sustain. Energy Fuels* **4**, 3143-3156, doi:10.1039/D0SE00524J (2020).

57 Toe, C. Y., Pan, J., Scott, J. & Amal, R. Identifying key design criteria for large-scale photocatalytic hydrogen generation from engineering and economic perspectives. *ACS EST Engg.* **2**, 1130-1143, doi:10.1021/acsestengg.2c00030 (2022).

58 Carr, A. J. & Pryor, T. L. A comparison of the performance of different PV module types in temperate climates. *Sol. Energy* **76**, 285-294, doi:https://doi.org/10.1016/j.solener.2003.07.026 (2004).

59 Li, J. *et al.* Electrocatalytic nitrate reduction to ammonia coupled with organic oxidation. *Chem Catal.* **3**, 100638, doi: https://doi.org/10.1016/j.checat.2023.100638 (2023).

60 Jain, M., Muthalathu, R. & Wu, X.-Y. Electrified ammonia production as a commodity and energy storage medium to connect the food, energy, and trade sectors. *iScience* **25**, 104724, doi:https://doi.org/10.1016/j.isci.2022.104724 (2022).

61 Leverett, J. *et al.* Tuning the coordination structure of Cu-N-C single atom catalysts for simultaneous electrochemical reduction of CO_2 and NO_3-to urea. *Adv. Energy Mater.* **12**, 2201500, doi: https://doi.org/10.1002/aenm.202201500 (2022).

62 Xiong, Y. *et al.* Electrochemical nitrate reduction: ammonia synthesis and the beyond. *Adv. Mater.* **36**, 2304021, doi: https://doi.org/10.1002/adma.202304021 (2024).

63 Zhou, P. *et al.* Solar-to-hydrogen efficiency of more than 9% in photocatalytic water splitting. *Nature* **613**, 66-70, doi:10.1038/s41586-022-05399-1 (2023).

64 Wang, D. *et al.* Oxygen-bridged copper–iron atomic pair as dual-metal active sites for boosting electrocatalytic NO reduction. *Adv. Mater.* **35**, 2304646, doi: https://doi.org/10.1002/adma.202304646 (2023).

65 Zhang, R. *et al.* A Zn–nitrite battery as an energy-output electrocatalytic system for high-efficiency ammonia synthesis using carbon-doped cobalt oxide nanotubes. *Energy Environ. Sci.* **15**, 3024-3032, doi:10.1039/D2EE00686C (2022).

66 Wilson, G. M. *et al.* The 2020 photovoltaic technologies roadmap. *J. Phys. D: Appl. Phys.* **53**, 493001, doi:10.1088/1361-6463/ab9c6a (2020).

67 Bobela, D. C., Gedvilas, L., Woodhouse, M., Horowitz, K. A. & Basore, P. A. Economic competitiveness of III–V on silicon tandem one-sun photovoltaic solar

modules in favorable future scenarios. *Prog. Photovolt: Res. Appl.* **25**, 41-48, doi: 10.1088/1361-6463/ab9c6a (2017).

68 Ghavam, S., Vahdati, M., Wilson, I. A. G. & Styring, P. Sustainable ammonia production processes. *Front. Energy Res.* **9**, 34, doi:10.3389/fenrg.2021.580808 (2021).